

ATI-CTLO: Adaptive Temporal Interval-based Continuous-Time LiDAR-Only Odometry

Bo Zhou, Jiajie Wu, Yan Pan and Chuanzhao Lu

Abstract—The motion distortion in LiDAR scans caused by the robot’s aggressive motion and environmental terrain feature significantly impacts the positioning and mapping performance of 3D LiDAR odometry. Existing distortion correction solutions struggle to balance computational complexity and accuracy. In this letter, we propose an Adaptive Temporal Interval-based Continuous-Time LiDAR-only Odometry, which based on straightforward and efficient linear interpolation. Our method can flexibly adjust the temporal intervals between control nodes according to the dynamics of motion and environmental degeneracy. This adaptability enhances performance across various motion states and improves the algorithm’s robustness in degenerate, particularly feature-sparse, environments. We validated our method’s effectiveness on multiple datasets across different platforms, achieving comparable accuracy to state-of-the-art LiDAR-only odometry methods. Notably, in situations involving aggressive motion and sparse features, our method outperforms existing LiDAR-only methods.

Index Terms—LiDAR-only odometry, continuous-time, motion distortion, degeneracy

I. INTRODUCTION

LiDAR odometry, recognized for its precise measurement capabilities and adaptability to changing light and weather conditions [1], has been extensively utilized in robotics and autonomous driving, showing remarkable progress over the last decade. Nonetheless, LiDAR odometry faces significant practical challenges, particularly the motion distortion in point clouds, which crucially affects localization accuracy and map-building quality. There are several sources of motion distortion, including robot motion during data acquisition, uneven terrain that causes the robot to oscillate, and environmental disturbances such as air currents affecting unmanned aerial vehicles (UAVs). Fig. 1 shows the motion distortion caused by aggressive turn during data acquisition and the mapping result of our method.

Most current LiDAR odometry methods are based on discrete-time methods, which assume LiDAR remains stationary during data acquisition and handle LiDAR distortion as part of preprocessing, aligning all points in a point cloud to a common reference frame based on constant velocity assumption [2], [3]. This method, while straightforward and efficient, is inadequate for more aggressive motions (As Fig. 1b shows, [3] still remains distortion). In LiDAR-inertial odometry (LIO) systems, IMUs are used to directly measure the poses of LiDAR points to eliminate distortions [4], [5]. However, this

This work was supported by the National Natural Science Foundation (NNSF) of China under Grant 620730075. (Corresponding author: Bo Zhou.)

All authors are with School of Automation, Southeast University, Nanjing 210096, P.R. China (email: zhoubo@seu.edu.cn; jiajiawu@seu.edu.cn; yanpan@seu.edu.cn; lucz@seu.edu.cn)

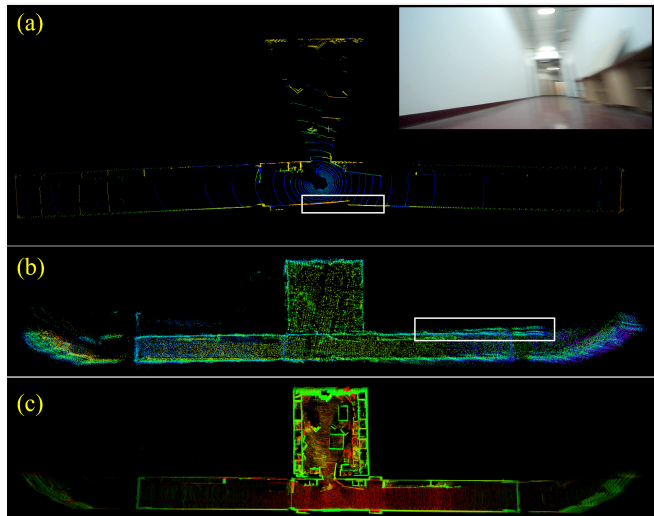


Fig. 1: **Motion distortion correction.** (a): A single frame of point cloud is distorted due to aggressive turning. (b): Correction distortion under constant velocity assumption (The mapping result of KISS-ICP [3]). (c): Our method, utilizing dynamic mapping interval control, ensures more accurate mapping.

requires precise calibration and is highly susceptible to platform vibrations, such as mechanical vibrations of quadruped robots [6], and is limited by the IMU’s measurement range in extreme motion conditions [7].

In contrast, continuous-time methods consider the LiDAR to be moving during data acquisition and model the trajectory as a function of time, allowing for pose queries at any given time, offering a new approach to correcting motion distortion. Current models often assume constant velocity [8]–[10] or higher-order modeling [11]–[13]. However, higher-order models increase computational complexity, while lower-order models suffer from reduced precision. One solution to this problem relies on the assumption of motion continuity, using lower-order modeling but with smaller temporal intervals between the control nodes [8], [14]. Small temporal interval allows the constant velocity motion prior to accommodate aggressive movements, but also introduces another problem. The small temporal intervals in continuous-time methods are often shorter than the duration of a single LiDAR frame, making it essential to segment the point cloud temporally. This segmentation reduces constraints between control nodes, leading to potential algorithm degeneracy or failure in feature-sparse environments.

To address aforementioned problems, we propose a continuous-time LiDAR-only method, the main contributions of our method are as follows:

- We introduce **ATI-CTLO** using linear interpolation, allowing for flexible adjustment of temporal intervals between control nodes compared to other methods based on linear interpolation. The approach decreases the interval based on the dynamics of motion and increases the interval when the degeneracy occurs, effectively balancing accuracy and real-time performance.
- To address the issue of degeneracy due to cloud segmentation, we introduce a degeneracy management method for continuous-time LiDAR odometry. By categorizing level of degeneracy based on the strength of environmental information constraints on the pose, we implement targeted treatments for each level. This approach significantly enhances the robustness of odometry in degenerate environments.
- The effectiveness of our method has been validated across datasets from multiple platforms. To our knowledge, this is the only LiDAR-only odometry approach that has been experimentally validated on Unmanned Ground Vehicles (UGVs), UAVs, and quadruped robots. The results shows a 10% improvement in positioning accuracy over the state-of-the-art (SOAT) methods. Moreover, in challenging environments, particularly those with sparse features, our algorithm outperforms all existing LiDAR-only odometry methods.

II. RELATED WORKS

A. Discrete-time and Continuous-time LiDAR Odometry

3D LiDAR odometry technology primarily estimates pose through point cloud registration. The classic method, Iterative Closest Point (ICP) algorithm [15], involves finding matching point pairs between the target and source point clouds and optimizing for the best transformation to minimize the distance between all pairs. In recent years, several outstanding works have enhanced ICP performance. For instance, KISS-ICP [3] proposed a lightweight ICP method that dynamically adjusts the data association threshold, adapting to multiple scenarios with just one parameter file. Feature-based methods achieve rapid and precise registration by extracting significant points from the point cloud. LOAM [16] is a representative of this approach, inspiring subsequent advancements like LeGO-LOAM [17], which incorporated ground optimization, and F-LOAM [2], which increased efficiency without sacrificing accuracy by adopting a scan-to-map method.

However, these methods rely on discrete-time representation, which inherently leads to LiDAR distortion issues. The common solutions involve using a constant velocity assumption or leveraging IMU pose estimation [4], [5]. Continuous-time trajectory methods offer an alternative approach to removing motion distortions in point clouds, which allow to query poses at any given time. Over the past decade, these techniques have made significant advancements in real-time performance and accuracy. Continuous-time methods can be divided into two main categories: nonparametric and parametric.

The nonparametric methods view the continuous-time trajectory as Gaussian process [18]–[20], the GP prior smooths

terms between discrete-time nodes. For parametric methods, B-spline is widely utilized to model the trajectory due to the locality and smoothness characteristics [21]. Thanks to the efficient derivative computation of cumulative B-splines [22], numerous high-performing B-spline-based continuous-time LiDAR(-IMU) odometry [11], [23] approaches have been developed. These approaches excel in handling point cloud motion distortion and improving the smoothness of the trajectory.

Besides these approaches, linear interpolation is also utilized for continuous trajectory modeling due to its efficiency and speed. CT-ICP [8] set poses at the start and end of each point cloud frame, using linear interpolation to fit the motion within the frame. However, it is not suitable for highly dynamic scenarios. Traj-LO [14] employed higher frequency pose controls to handle more aggressive movements, though this reduces the observational constraints between control nodes. To overcome the disadvantages of fixed control nodes, Coco-LIC [24] integrated non-uniform B-splines, dynamically adjusting B-control nodes through IMU pre-estimation of motion. Nevertheless, this approach relies on IMU pre-estimation and suffers from reduced observational data in high-frequency interpolation scenarios.

B. Degeneracy Detection

LiDAR odometry is highly susceptible to degeneracy in environments with sparse or repetitive geometric features. Continuous-time LiDAR odometry, which uses smaller time intervals for more accurate trajectory fitting, exacerbates the risk of degeneracy due to the reduced number of LiDAR points between adjacent control nodes. Hence, degeneracy detecting is essential for improving the robustness of LiDAR odometry.

Zhang et al. [25] determined degeneracy by comparing the smallest eigenvalue λ_{min} of the Hessian matrix to a predefined threshold, separating the degenerate directions in the state space and optimizing only in well-constrained directions. Hinduja et al. [26] applied this method to ICP, and using the ratio between the largest and smallest eigenvalues as the eigenvalue threshold. Ren et al. [27] suggested that pose updates in the degenerate direction cause oscillations and calculates the covariance matrix of pose updates during optimization, summing the diagonal elements as the degeneracy factor. Nubert et al. [28] introduced a learning-based degeneracy detection method, directly estimating localizability on raw LiDAR scans.

Another approach directly identifies the degenerate directions through the geometric characteristics of environment. Yang et al. [29] utilized PCA to analyze the normal vectors of all points in the point cloud, also using the smallest eigenvalue λ_{min} as a criterion for describing degeneracy. Zhen et al. [30] evaluated the strength of the constraint by measuring the sensitivity of measurements w.r.t the robot pose, but the method requires a prior-build map of the environment. X-ICP [31] employed a similar method to [30], evaluated the contribution of information pairs to the constraints. The method categorized localizability into three levels $\{localizable, partially local-$

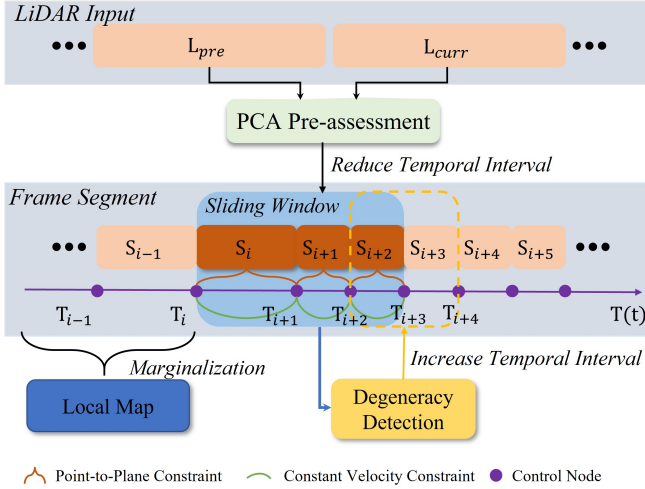


Fig. 2: **System Overview.** Firstly, LiDAR scans segmentation is based on PCA assessment, followed by solving through sliding window approach. Simultaneously, degeneracy management merges cloud segments when degeneracy occurs.

izable, nonlocalizable} and enhanced constraints for partial localizability through resampling the available information.

III. METHODOLOGY

A. System Overview

The Fig.2 shows our pipeline. We denote the trajectory as $T(t)$ in world frame, which is composed of continuous linear segments $[T_i, T_{i+1})$ over interval $[t_i, t_{i+1})$, the Lie Group T_i represents the pose at timestamp t_i . For the latest LiDAR input point cloud L_{curr} , PCA technique is first used to evaluate the angle φ between the principal directions of L_{curr} and the previous point cloud L_{pre} . Then the temporal interval Δt between control nodes is reduced by a certain factor α once the angle φ exceeds the predefined threshold (Section III-B). After setting the temporal interval Δt , the points in L_{curr} are divided into cloud segments $\{S_{i+1}, S_{i+2}, \dots, S_{i+5}\}$ according to their timestamps. A sliding window approach is utilized to optimize multiple segments $\{S_i, S_{i+1}, S_{i+2}\}$ at once, Once the optimization is finished, the slide window shifts backward to include new linear segments, while the oldest segment is added to the local map (Section III-C). Notably, during the iterative optimization, the degeneracy detection module is applied to determine if the time interval should be increased, which is then achieved by merging linear segments (Section III-D).

B. PCA Pre-assessment to Reduce Temporal Interval

The first-order linear motion model is straightforward and efficient but introduces significant errors during aggressive motions. To address this, higher-order motion models can be used, although they tend to be redundant and waste computational resources in stable conditions. Another approach involves using denser node configurations to handle aggressive motions. Therefore, predicting rapid motion changes is critical for effective node placement. Coco-LIC [24] used IMU

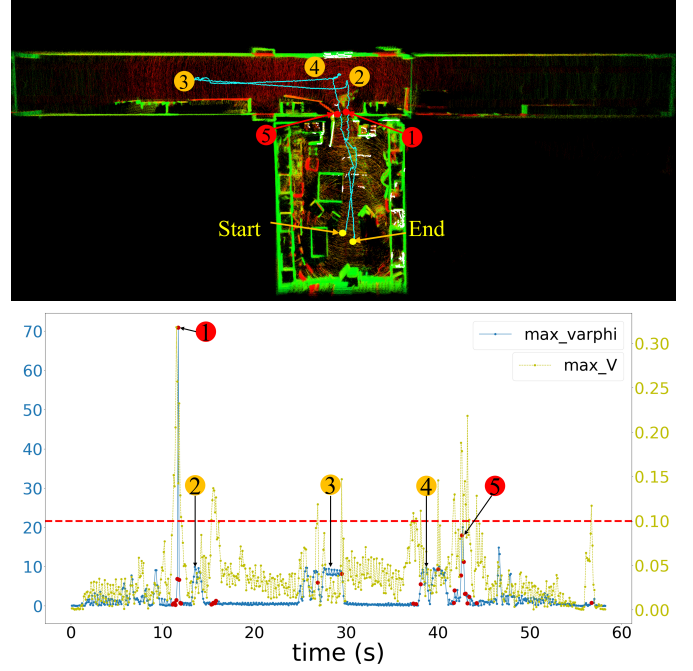


Fig. 3: **PCA pre-assessment.** A sudden change in the eigenvectors v_i indicates a aggressive turn in motion. In the **upper image**, the nodes with numbers show significant changes in the PCA direction. However, only the yellow nodes (2, 3, 4) are due to motion turns, while the red nodes (1, 5) result from environmental changes (e.g., the robot moving from a room into a hallway, or vice versa). The **line chart** below records the maximum PCA direction change φ_{max} (max_varphi, blue) and the maximum eigenvalue change V_{max} (max_V, yellow) throughout the entire trajectory. At nodes 1 and 5, there is a significantly change in V_{max} , and we filter out erroneous estimates (red nodes) by setting a threshold (red line).

measurements for preliminary estimates, but for LiDAR-only odometry, the key challenge is to quickly estimate motion states based solely on LiDAR scans.

Inspired by the scan-to-scan principle in [16], we use the matching of the current and previous LiDAR frames to acquire pose transformations. However, differing from the discrete-time method, our scan-to-scan method requires only a rough description of motion changes, not the exact pose transformation between frames, since the kinematic constraints have provided pose priors. Principal Component Analysis (PCA) is used to extract the main direction of the point cloud, with changes in this principal direction indicating the degree of pose change. As shown in Fig. 3, during the robot's turning process (yellow nodes 2, 3, 4), the principal direction of the point cloud undergoes significant changes (blue). Note that we only concentrate on the changes in the principal direction caused by violent rotations, since constant velocity prior introduces significant errors when such rotations occur.

For the j -th point L_{p_j} in N points in L_{curr} , we first

compute the covariance matrix $\mathbf{C} \in \mathbb{R}^{3 \times 3}$ of all points:

$$\mathbf{C} = \sum_{j=1}^N ({}^L \mathbf{p}_j - \bar{\mathbf{p}})^\top ({}^L \mathbf{p}_j - \bar{\mathbf{p}}) \quad (1a)$$

$$\bar{\mathbf{p}} = \frac{1}{N} \sum_{j=1}^N {}^L \mathbf{p}_j \quad (1b)$$

Then Singular Value Decomposition (SVD) is applied to \mathbf{C} to derive the eigenvalues $\lambda_0 < \lambda_1 < \lambda_2$ and corresponding eigenvectors $\mathbf{v}_0, \mathbf{v}_1, \mathbf{v}_2$. The eigenvectors represent the principle directions of LiDAR scans, so the angles $\varphi = [\varphi_1, \varphi_2, \varphi_3]$ between the principle directions $\mathbf{v}^{curr}, \mathbf{v}^{last}$ of adjacent LiDAR scans indicate the dynamics of motion.

$$\varphi_i = \arccos\left(\frac{\mathbf{v}_i^{curr} \cdot \mathbf{v}_i^{last}}{\|\mathbf{v}_i^{curr}\| \|\mathbf{v}_i^{last}\|}\right), i = 0, 1, 2 \quad (2)$$

However, the principal directions derived from PCA can abruptly change due to changes in the environment. During our experiments, we observed that these environmental changes also lead to variations in the eigenvalues, which can be seen in Fig. 3. Leveraging this observation, we filter out changes in the PCA principal direction resulting from environmental changes:

$$\mathcal{V}_{max} = \max\left(\frac{\lambda_i^{curr}}{\lambda_i^{last}} - 1\right), i = 0, 1, 2 \quad (3a)$$

$$\varphi_{final} = \begin{cases} \varphi, & \mathcal{V}_{max} < \mathcal{K}_{val} \\ \mathbf{0} \in \mathbb{R}^{3 \times 1}, & otherwise \end{cases} \quad (3b)$$

Only when the max change \mathcal{V}_{max} in eigenvalues falls within a specified threshold \mathcal{K}_{val} do we consider the principal direction change to be caused by motion. We analyze the final φ_{final} by comparing the max element φ_{max} with the certain threshold \mathcal{K}_{vec} . If φ_{max} exceeds \mathcal{K}_{vec} , we reduce the temporal interval by a predetermined factor α .

C. Non-Uniform Linear Interpolation Continuous-time LiDAR-Only Odometry based on Sliding Window

The continuous-time LiDAR odometry addresses the following problem: given the cloud segments $\mathbf{S}_i, i = 0, 1, 2, \dots$, estimate the corresponding linear segments $[\mathbf{T}_i, \mathbf{T}_{i+1}]$ in the continuous trajectory $\mathbf{T}(t)$. Each linear segment $[\mathbf{T}_i, \mathbf{T}_{i+1}]$ is solved through point-to-plane registration, constant velocity constraint. In summary, we solve the following problem to get the control nodes $\mathbf{X} = (\mathbf{T}_i, \mathbf{T}_{i+1}, \dots, \mathbf{T}_{i+M})$ in the sliding window, M is the capacity of sliding window:

$$\arg \min_{\mathbf{X}} \mathcal{F}(\mathbf{X}) = \arg \min_{\mathbf{X}} \mathcal{F}_{ptpl}(\mathbf{X}) + \mathcal{F}_{vel}(\mathbf{X}) + \mathcal{F}_m(\mathbf{X}) \quad (4)$$

where the $\mathcal{F}_{ptpl}(\mathbf{X})$ is the point-to-plane registration errors, $\mathcal{F}_{vel}(\mathbf{X})$ is the constant velocity constraint. $\mathcal{F}_m(\mathbf{X})$ is the marginalization energy which keeps information of the removed variables when the sliding window slides. The error functions $\mathcal{F}_{ptpl}(\mathbf{X})$ and $\mathcal{F}_{vel}(\mathbf{X})$ of the whole sliding window

consists of M sub-error functions:

$$\mathcal{F}_{ptpl}(\mathbf{X}) = \sum_{k=0}^{M-1} \mathcal{F}_{ptpl}(\mathbf{T}_{i+k}, \mathbf{T}_{i+k+1}) \quad (5a)$$

$$\mathcal{F}_{vel}(\mathbf{X}) = \sum_{k=0}^{M-1} \mathcal{F}_{vel}(\mathbf{T}_{i+k}, \mathbf{T}_{i+k+1}) \quad (5b)$$

Every single sub-error function is associated with the linear segment $[\mathbf{T}_{i+k}, \mathbf{T}_{i+k+1}]$ and the cloud segment \mathbf{S}_{i+k} . For the point-to-plane constraint:

$$\mathcal{F}_{ptpl}(\mathbf{T}_{i+k}, \mathbf{T}_{i+k+1}) = \mathbf{e}_p(i+k) \mathbf{Q}_p^{-1} \mathbf{e}_p(i+k) \quad (6a)$$

$$\mathbf{e}_p(i+k) = \sum_{j=1}^{N_s} \mathbf{n}_{q_j}^T (\mathbf{T}_j \cdot {}^L \mathbf{p}_j - {}^W \mathbf{q}_j) \quad (6b)$$

where ${}^L \mathbf{p}_j$ is the j -th point of N_s time-ordered points in \mathbf{S}_{i+k} , \mathbf{T}_j transforms the point ${}^L \mathbf{p}_j$ to ${}^W \mathbf{p}_j$. ${}^W \mathbf{q}_j$ is the closest point to ${}^W \mathbf{p}_j$ in local map, and \mathbf{n}_{q_j} denotes the normal vector of plane that includes ${}^W \mathbf{q}_j$. Then we calculate the error $\mathbf{e}_p(i+k) \sim \mathcal{N}(\mathbf{0}, \mathbf{Q}_p)$. Due to the constant velocity prior, \mathbf{T}_j is calculated via linear interpolation as follows:

$$\mathbf{T}_j = \mathbf{T}_{i+k} \cdot \text{Exp}(\alpha_j \cdot \text{Log}(\mathbf{T}_{i+k}^{-1} \mathbf{T}_{i+k+1})) \quad (7a)$$

$$\alpha_j = (t_j - t_{i+k}) / (t_{i+k+1} - t_{i+k}) \quad (7b)$$

As for $\mathcal{F}_{vel}(\mathbf{T}_{i+k}, \mathbf{T}_{i+k+1})$, we first calculate the kinematic error $\mathbf{e}_v(i+k) \sim \mathcal{N}(\mathbf{0}, \mathbf{Q}_v)$. Due to the varying intervals between adjacent linear segments, a scaling factor γ_{i+k} must be incorporated into the constraint calculations:

$$\mathcal{F}_{vel}(\mathbf{T}_{i+k}, \mathbf{T}_{i+k+1}) = \mathbf{e}_v^\top(i+k) \mathbf{Q}_v^{-1} \mathbf{e}_v(i+k) \quad (8a)$$

$$\mathbf{e}_v(i+k) =$$

$$\text{Log}(\mathbf{T}_{i+k}^{-1} \mathbf{T}_{i+k+1}) - \gamma_{i+k} \cdot \text{Log}(\mathbf{T}_{i+k-1}^{-1} \mathbf{T}_{i+k}) \quad (8b)$$

$$\gamma_{i+k} = (t_{i+k+1} - t_{i+k}) / (t_{i+k} - t_{i+k-1}) \quad (8c)$$

When the sliding window slides forward, old control nodes \mathbf{X}_m are removed through marginalization, While the corresponding cloud segments \mathbf{S}_m are added to local map. The energy \mathcal{F}_m keeps information from \mathbf{X}_m , which is commonly stored as:

$$\mathcal{F}_m = \frac{1}{2} (\mathbf{X}_m - \mathbf{X}_m^0)^\top H_m (\mathbf{X}_m - \mathbf{X}_m^0) + b_m^\top (\mathbf{X}_m - \mathbf{X}_m^0) \quad (9a)$$

$$H_m = J_m^\top J_m, \quad b_m = J_m^\top r_m \quad (9b)$$

where the H_m, b_m is marginalization priors, the \mathbf{X}_m^0 is the linearization point of the removed nodes, which is applied for calculating the *Schur complement* \tilde{H} and corresponding vector \tilde{b} . From the H_m, b_m , we can derive J_m and r_m as (9b), please refer to [14] for more details.

D. Degeneracy Management to Increase Temporal Interval

1) *Degeneracy Detection*: As the linear segments \mathbf{S}_i are obtained by slicing the LiDAR scans \mathbf{L} , they accumulate fewer LiDAR points compared to discrete-time methods, which increases the likelihood of degeneracy during optimization. In this paper, a classification of degeneracy levels was conducted using geometric feature-based methods, with specific handling

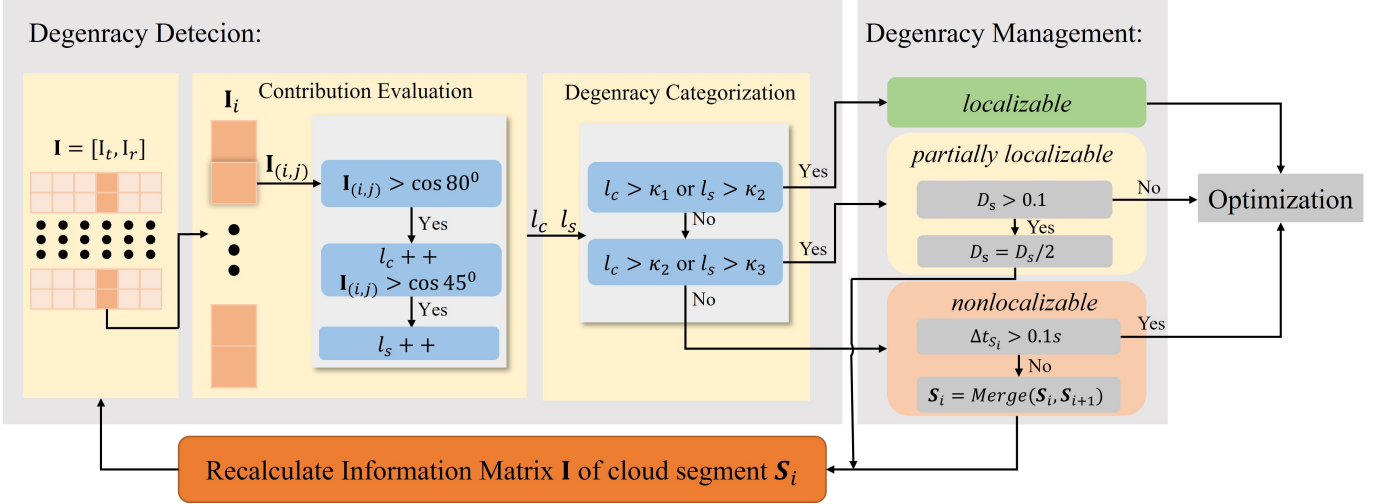


Fig. 4: **Degeneracy Detection:** Each column of the information matrix \mathbf{I} represents the projection of environmental information in the corresponding pose direction. In the contribution evaluation, we calculate the contribution of each column \mathbf{I}_i and use l_c and l_s to count the number of information elements $\mathbf{I}_{(i,j)}$ with varying levels of contribution. Then different thresholds $\kappa_1, \kappa_2, \kappa_3$ are used to classify the contributions into various levels, eventually the localizability of each direction is divided into three levels: $\{localizable, partially\ localizable, nonlocalizable\}$. **Degeneracy Management:** we enhance the number of effective information elements by increasing the sampling rate (decreasing D_s) for partially localizable direction. In nonlocalizable case, subsequent cloud segment \mathbf{S}_{i+1} is merged to gather more valid information.

approaches applied to each level. This approach evaluates how much a information pair (${}^L\mathbf{p}, {}^L\mathbf{n}$) contributes the localizability towards principle directions in optimization. Similar to [31], the normal vector ${}^L\mathbf{n}$ and torque $\boldsymbol{\tau} = {}^L\mathbf{p} \times {}^L\mathbf{n}$ in LiDAR frame respectively provide localizability contributions toward translational \mathbf{v}_t and rotational \mathbf{v}_r directions, which are the eigenvectors of Hessian matrix of optimization. When the normal vector ${}^L\mathbf{n}$ or torque $\boldsymbol{\tau}$ aligns with the principal directions of optimization (${}^L\mathbf{n} \cdot \mathbf{v}_t > 0$ or $\boldsymbol{\tau} \cdot \mathbf{v}_r > 0$), it is deemed to provide a localizability contribution. Due to the point ${}^L\mathbf{p}$ can be at long distance, the $\boldsymbol{\tau}$ need to be normalized first, so the information matrix is as:

$$\mathbf{F}_r = \begin{bmatrix} \frac{\boldsymbol{\tau}_1}{\|\boldsymbol{\tau}_1\|_2} & \cdots & \frac{\boldsymbol{\tau}_n}{\|\boldsymbol{\tau}_n\|_2} \end{bmatrix}^\top, \mathbf{F}_t = [{}^L\mathbf{n}_1 \quad \cdots \quad {}^L\mathbf{n}_n]^\top \quad (10)$$

In this letter, the sliding window is used to optimize several linear segments at once, but it is unnecessary to evaluate all information pairs within the window as it can lead to repeated assessments of the same linear segment. As Fig. 2 shows, for each optimization, we only focus on the latest cloud segment \mathbf{S}_{i+2} . We perform SVD decomposition of the Hessian Matrix of \mathbf{T}_{i+3} to obtain the principal direction matrices of rotation \mathbf{V}_r and translation \mathbf{V}_t . By projecting the information matrices \mathbf{F} onto the main optimization directions \mathbf{V} , we can determine the contributions in each respective direction:

$$\mathbf{I}_r = (\mathbf{F}_r \cdot \mathbf{V}_r)^{|\cdot|} \in \mathbb{R}^{n \times 3}, \quad \mathbf{I}_t = (\mathbf{F}_t \cdot \mathbf{V}_t)^{|\cdot|} \in \mathbb{R}^{n \times 3} \quad (11)$$

The $|\cdot|$ means getting the absolute value of all elements in matrix. In matrix $\mathbf{I} = [\mathbf{I}_t, \mathbf{I}_r]$ indicates the contribution level of information pair (${}^L\mathbf{p}_i, {}^L\mathbf{n}_i$) to direction \mathbf{v}_{r_j} or \mathbf{v}_{t_j} . We then divide the localizability of each direction into three levels by evaluating the contribution of information matrix, more details can be seen in Fig. 4.

2) *Degeneracy Management:* In discrete-time methods, the nonlocalizable directions are excluded from the optimization, and prior motions values are used instead. For partially localizable directions, the constraints are calculated by resampling the available information instead.

In this letter, degeneracy may arise from the segmentation of the point cloud, which reduces the number of constraint points. Thus, we must first exclude degeneracy caused by this factor. As Fig. 4 shows, if a particular direction is nonlocalizable, we will merge the \mathbf{S}_i with the next segment \mathbf{S}_{i+1} and then perform degeneracy detection again. To prevent unlimited merging, we stop the process when the temporal interval Δt_{S_i} of segment \mathbf{S}_i exceeds 0.1 seconds. If a direction is partially localizable, it indicates that \mathbf{S}_i contains useful information. We then halve the voxel size for downsampling \mathbf{S}_i to obtain more available information pairs. Similarly, when the voxel size falls below 0.1, we move directly to the optimization.

IV. EXPERIMENTS

We validated the effectiveness of the ATI-CTLO algorithm on datasets from various platforms, including UGV dataset M2DGR [32], UAV dataset NTU VIRAL [33] and our own quadruped robot dataset. In comparisons with the state-of-the-art LiDAR odometry methods, including discrete-time methods LeGO-LOAM and KISS-ICP, and fixed-interval continuous-time odometry algorithms like CT-ICP and Traj-LO, our method ATI-CTLO demonstrated an ability to handle more challenging environments while improving accuracy by around 10% in ground robots.

In this letter, we maintained the same parameters setting for all experiments. In the PCA pre-assessment module, when the change in eigenvalue is below $\mathcal{K}_{val} = 0.1$ and the angle φ_{max} exceeds $\mathcal{K}_{vec} = 10$, we halve the temporal interval ($\alpha = 0.5$). In the degeneracy management module, we use $\kappa_1 =$

TABLE I: ATE of LiDAR-Only Odometry on M2DGR Dataset

Approach	street_03	street_07	room_01	room_dark_06	gate_01	hall_02	door_02	circle_01	average
LeGO_LOAM	0.597	10.584	0.136	0.305	0.328	0.239	0.187	1.529	1.738
KISS-ICP	0.131	0.400	0.219	0.339	0.141	0.276	0.263	1.499	0.408
CT-ICP	0.174	x	0.144	0.293	0.159	0.259	0.211	0.357	0.228
Traj-LO	0.173	0.249	0.148	0.293	0.151	0.257	0.196	0.357	0.228
ours	0.170	0.212	0.132	0.284	0.151	0.251	0.185	0.354	0.186

TABLE II: NTU VIRAL Dataset

Approach	Sensor	eee			nya			sbs			rtp			tnp			spms		
		01	02	03	01	02	03	01	02	03	01	02	03	01	02	03	01	02	03
FLOAM	L1	4.486	8.328	1.133	1.447	1.292	1.498	0.976	0.2010	1.079	10.775	4.637	2.218	2.354	2.249	1.566	x	x	x
KISS-ICP	L1	2.220	1.570	1.014	0.628	1.500	1.272	0.917	1.312	1.030	3.663	1.970	2.382	2.305	2.405	0.799	8.493	x	5.454
CT-ICP	L1	7.763	0.125	11.171	0.100	0.101	0.073	x	0.084	1.545	x	0.081	0.086	0.073	0.071	0.045	x	x	x
Traj-LO	L1	0.055	0.039	0.035	0.047	0.052	0.050	0.048	0.039	0.039	0.050	0.058	0.057	0.505	0.607	0.101	0.121	x	0.103
ours	L1	0.046	0.033	0.031	0.044	0.048	0.047	0.032	0.030	0.032	0.054	0.058	0.056	0.378	0.360	0.091	0.072	0.077	0.079

125, $\kappa_2 = 50, \kappa_3 = 15$ to classify the levels of degeneracy. All experiments were conducted on a Intel i7-12700H CPU.

A. Dataset Result

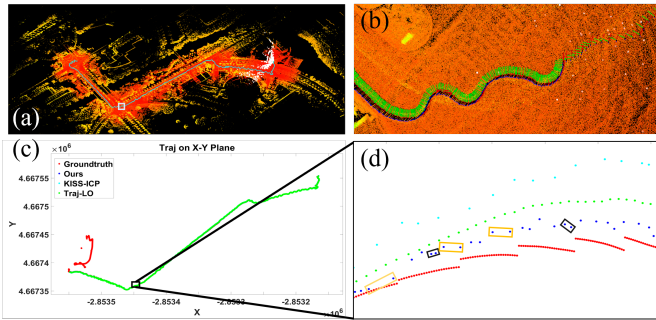


Fig. 5: Results of LiDAR odometry on *street_07* sequence of M2DGR. (a) Our method, the yellow box marks the position where CT-ICP drifts. (b) CT-ICP drifts. (c) Trajectory results aligned with the ground truth. (d) A zoomed-in view, where orange boxes indicates increased temporal intervals between control nodes due to degeneracy management, and black boxes indicates reduced intervals due to PCA-assessed motion state changes

1) *M2DGR Dataset*: We first validate our algorithm’s effectiveness under vehicle conditions. The M2DGR dataset, collected by a UGV (Unmanned Ground Vehicle), provided data from various environments. We conduct tests in each environment and compute the RMSE of ATE error for the trajectories. The results are shown in Table I, showing that our method achieved an approximate 10% improvement in average accuracy compared to the state-of-the-art (SOTA) LiDAR-Only methods (excluding the *street_07* sequence for average accuracy of CT-ICP). In sequences such as *street_03*, *gate_01*, and *hall_02*, where the vehicle’s movement is relatively smooth, discrete-time methods outperform continuous-time methods in terms of accuracy. However, in sequences with aggressive turns, such as *street_07* and *circle_01*, the errors of discrete-time methods increase significantly. Across all sequences, continuous-time methods maintain more stable accuracy, and our method consistently achieve the highest accuracy among continuous-time methods. This improvement is due to our dynamic temporal interval adjustment strategy.

As seen in Fig. 5(d), our method continuously adjusts the time intervals, resulting in a more accurate alignment with the ground truth. In contrast, CT-ICP experiences significant drift during execution (Fig. 5(b)), leading to automatic termination.

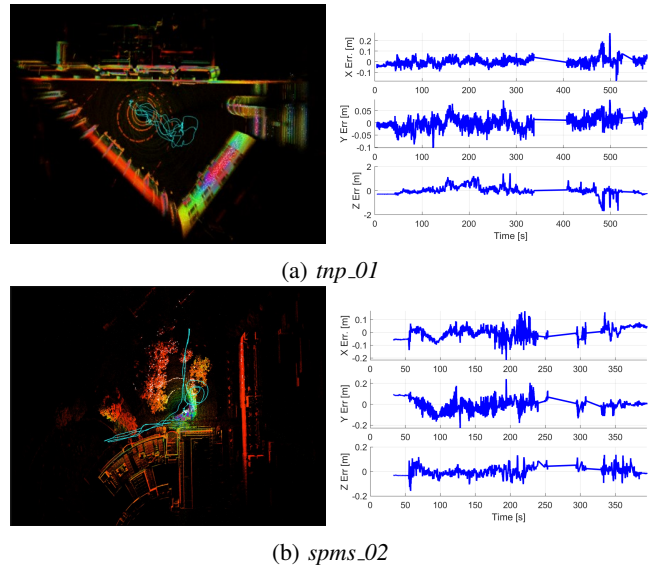


Fig. 6: The environments and errors of our method on *tnp_01* and *spms_02* sequences. The Z-axis error is significantly greater than the X and Y axes, indicating that most trajectory errors stem from the Z-axis.

2) *NTU VIRAL Dataset*: The NTU VIRAL dataset records multiple sequences in several challenging indoor and outdoor conditions by an UAV, which equipped with two Ouster LiDAR: one horizontal (L1) and one vertical (L2). All algorithms are tested using the L1 LiDAR, and error evaluations are based on scripts provided by the dataset authors¹. Since LeGO-LOAM is designed for ground robots, we employ another feature-based method F-LOAM instead. As shown in Table II, our algorithm achieve the highest accuracy in sequences *eee*, *nya*, *sbs*, *rtp*.

The *tnp* sequences are recorded in a courtyard surrounded by three buildings, where the features in the z-axis direction

¹https://ntu-aris.github.io/ntu_viral_dataset/evaluation_tutorial.html

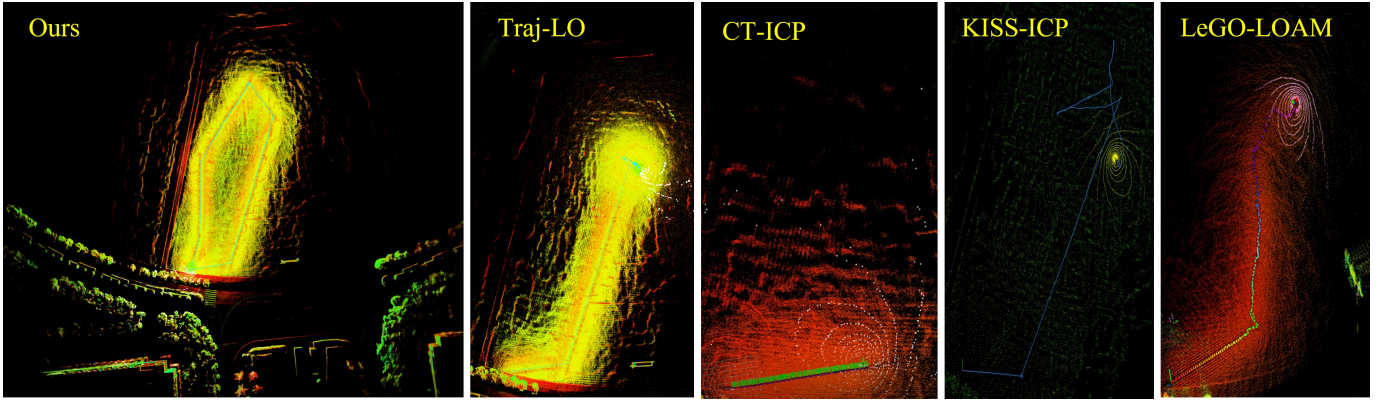


Fig. 7: Results on *hard* sequences. Our method is the only algorithm that successfully completed the *hard* sequence among tested methods.



Fig. 8: Jueying Lite2 and Jiulonghu Campus Dataset.

are similar, and the horizontally placed L1 LiDAR provided fewer constraints on the z-axis compared to the x and y axes, exacerbating errors in the z-axis. In CT-ICP, each trajectory segment $[\mathbf{T}_i, \mathbf{T}_{i+1}]$ is constrained by the corresponding complete LiDAR scan, offering more comprehensive constraints. Conversely, in our approach and Traj-LO, the segmentation of the point cloud results in significant vertical errors due to the similarity of local information in the horizontal direction. However, our approach to handling degeneracy effectively mitigates this negative impact, resulting in higher accuracy compared to Traj-LO. Fig. 6(a) shows the error components for each axis and environment of *tnp_01*.

In the *spms* sequences, the UAV flies away from the buildings, resulting in a lack of LiDAR points, causing the failure of most algorithms. Traj-LO exhibits robustness by ensuring odometry convergence through kinematic constraints. However, in the *spms_02* sequence, it ultimately fails when the LiDAR points between control nodes become excessively sparse. In contrast, our method can detect degeneracy due to sparse LiDAR points and merges subsequent point cloud segments, ensuring a sufficient number of LiDAR points between control nodes, results are shown in Fig. 6(b).

3) *Our Own Jiulonghu Campus Dataset*: In addition to public datasets, we validate the effectiveness of our method under challenge conditions. As shown in the Fig. 8, using the quadruped robot *Jueying Lite2*, equipped with a Robosense RS-Helios 32-line LiDAR, we collect challenging sequences on the lawn of Southeast University’s *Jiulonghu* Campus. The sequences labeled *easy*, *medium*, and *hard* increase in difficulty and distance from the lawn edge. In the easy sequence, the robot moves along the lawn’s edge. In the medium sequence, the robot moves towards the center of the lawn but still has some trees and other obstacles providing

LiDAR points. In the hard sequence, the robot is in the middle of the lawn, surrounded only by the ground and sparse edge points, leading to significant degeneracy.

TABLE III: Jiulonghu Campus Dataset Results

Sequences	LeGO-LOAM	KISS-ICP	CT-ICP	Traj-LO	Ours
easy	✗	✓	✗	✓	✓
medium	✗	✗	✗	✓	✓
hard	✗	✗	✗	✗	✓

As shown in Table III, among the tested LiDAR-only odometry algorithms, ours is the only one that successfully completes all sequences. LeGO-LOAM and CT-ICP are unable to complete any test, while KISS-ICP manages to pass the *easy* sequences. Traj-LO manages well in *easy* and *medium* conditions but fails in *hard* sequence due to sparse feature points. Fig. 7 shows the result on *hard* sequence, CT-ICP experiences significant drift during aggressive turns, causing the program to terminate automatically. LeGO-LOAM drifts when moving towards the center of the lawn as the edge features gradually diminish. KISS-ICP and Traj-LO fail to handle changes in motion state when features are sparse. Our approach not only incorporates kinematic constraints but also dynamically increases temporal intervals during degeneracy, addressing the reduction of LiDAR information caused by cloud segmentation in continuous-time methods.

B. Real-Time Analysis

TABLE IV: The Pose Output Temporal Interval

Sequences	<i>street_07</i>	<i>spms_02</i>	<i>hard</i>
Average Interval(ms)	64.16	82.89	48.78

Our method dynamically adjusts the temporal interval between control nodes, resulting in a non-fixed pose output frequency. We evaluated the pose output frequency across sequences from three platforms. As depicted in the Table IV, the *street_07* sequence is a standard road scene with continuous aggressive turns, yielding an average pose output rate of 64.16ms. In the *spms_02* environment, degeneracy requires continuous cloud segment fusion, resulting in a lower output rate (82.89ms). In contrast, the *hard* sequence from the

Jiulonghu Campus Dataset, despite continuous cloud segment fusion, has sparser environmental features leading to a higher output rate (48.78ms). The overall pose output rate of our method falls between 10Hz and 20Hz.

V. CONCLUSIONS

We introduce an adaptive continuous-time LiDAR odometry that dynamically adjusts the temporal intervals between control nodes based on motion dynamics and environmental features, offering significant advantages in handling more aggressive motions and open environments. The degeneracy management approach successfully addresses the degeneracy problems arising from point cloud segmentation in existing continuous-time methods. Experiments on various platforms demonstrate that our method achieves accuracy comparable to current SOTA methods and outperforms them in feature-sparse environments. Future work will focus on continuous-time loop detection techniques to enhance the performance of continuous-time methods in long-duration navigation scenarios.

REFERENCES

- [1] D. Lee, M. Jung, W. Yang, and A. Kim, "Lidar odometry survey: recent advancements and remaining challenges," *Intelligent Service Robotics*, pp. 1–24, 2024.
- [2] H. Wang, C. Wang, C.-L. Chen, and L. Xie, "F-loam: Fast lidar odometry and mapping," in *2021 IEEE/RSJ International Conference on Intelligent Robots and Systems (IROS)*, pp. 4390–4396, IEEE, 2021.
- [3] I. Vizzo, T. Guadagnino, B. Mersch, L. Wiesmann, J. Behley, and C. Stachniss, "Kiss-icp: In defense of point-to-point icp—simple, accurate, and robust registration if done the right way," *IEEE Robotics and Automation Letters*, vol. 8, no. 2, pp. 1029–1036, 2023.
- [4] T. Shan, B. Englot, D. Meyers, W. Wang, C. Ratti, and D. Rus, "Lio-sam: Tightly-coupled lidar inertial odometry via smoothing and mapping," in *2020 IEEE/RSJ international conference on intelligent robots and systems (IROS)*, pp. 5135–5142, IEEE, 2020.
- [5] W. Xu, Y. Cai, D. He, J. Lin, and F. Zhang, "Fast-lio2: Fast direct lidar-inertial odometry," *IEEE Transactions on Robotics*, vol. 38, no. 4, pp. 2053–2073, 2022.
- [6] S. Yang, Z. Zhang, Z. Fu, and Z. Manchester, "Cerberus: Low-drift visual-inertial-leg odometry for agile locomotion," in *2023 IEEE International Conference on Robotics and Automation (ICRA)*, pp. 4193–4199, IEEE, 2023.
- [7] D. He, W. Xu, N. Chen, F. Kong, C. Yuan, and F. Zhang, "Point-lio: Robust high-bandwidth light detection and ranging inertial odometry," *Advanced Intelligent Systems*, vol. 5, no. 7, p. 2200459, 2023.
- [8] P. Dellenbach, J.-E. Deschaud, B. Jacquet, and F. Goulette, "Ct-icp: Real-time elastic lidar odometry with loop closure," in *2022 International Conference on Robotics and Automation (ICRA)*, pp. 5580–5586, IEEE, 2022.
- [9] T.-M. Nguyen, D. Duberg, P. Jensfelt, S. Yuan, and L. Xie, "Slic: Multi-input multi-scale surfel-based lidar-inertial continuous-time odometry and mapping," *IEEE Robotics and Automation Letters*, vol. 8, no. 4, pp. 2102–2109, 2023.
- [10] X. Zheng and J. Zhu, "Ectlo: Effective continuous-time odometry using range image for lidar with small fov," in *2023 IEEE/RSJ International Conference on Intelligent Robots and Systems (IROS)*, pp. 9102–9109, IEEE, 2023.
- [11] D. Droschel and S. Behnke, "Efficient continuous-time slam for 3d lidar-based online mapping," in *2018 IEEE International Conference on Robotics and Automation (ICRA)*, pp. 5000–5007, IEEE, 2018.
- [12] J. Quenzel and S. Behnke, "Real-time multi-adaptive-resolution-surfel 6d lidar odometry using continuous-time trajectory optimization," in *2021 IEEE/RSJ International Conference on Intelligent Robots and Systems (IROS)*, pp. 5499–5506, IEEE, 2021.
- [13] K. Chen, R. Nemiroff, and B. T. Lopez, "Direct lidar-inertial odometry: Lightweight lio with continuous-time motion correction," in *2023 IEEE International Conference on Robotics and Automation (ICRA)*, pp. 3983–3989, IEEE, 2023.
- [14] X. Zheng and J. Zhu, "Traj-lo: In defense of lidar-only odometry using an effective continuous-time trajectory," *IEEE Robotics and Automation Letters*, 2024.
- [15] P. J. Besl and N. D. McKay, "Method for registration of 3-d shapes," in *Sensor fusion IV: control paradigms and data structures*, vol. 1611, pp. 586–606, Spie, 1992.
- [16] J. Zhang and S. Singh, "Loam: Lidar odometry and mapping in real-time.," in *Robotics: Science and systems*, vol. 2, pp. 1–9, Berkeley, CA, 2014.
- [17] T. Shan and B. Englot, "Lego-loam: Lightweight and ground-optimized lidar odometry and mapping on variable terrain," in *2018 IEEE/RSJ International Conference on Intelligent Robots and Systems (IROS)*, pp. 4758–4765, IEEE, 2018.
- [18] S. Anderson and T. D. Barfoot, "Full steam ahead: Exactly sparse gaussian process regression for batch continuous-time trajectory estimation on se (3)," in *2015 IEEE/RSJ International Conference on Intelligent Robots and Systems (IROS)*, pp. 157–164, IEEE, 2015.
- [19] J. Dong, M. Mukadam, B. Boots, and F. Dellaert, "Sparse gaussian processes on matrix lie groups: A unified framework for optimizing continuous-time trajectories," in *2018 IEEE International Conference on Robotics and Automation (ICRA)*, pp. 6497–6504, IEEE, 2018.
- [20] C. Le Gentil, T. Vidal-Calleja, and S. Huang, "In2lama: Inertial lidar localisation and mapping," in *2019 International Conference on Robotics and Automation (ICRA)*, pp. 6388–6394, IEEE, 2019.
- [21] G. Cioffi, T. Cieslewski, and D. Scaramuzza, "Continuous-time vs. discrete-time vision-based slam: A comparative study," *IEEE Robotics and Automation Letters*, vol. 7, no. 2, pp. 2399–2406, 2022.
- [22] C. Sommer, V. Usenko, D. Schubert, N. Demmel, and D. Cremers, "Efficient derivative computation for cumulative b-splines on lie groups," in *Proceedings of the IEEE/CVF conference on computer vision and pattern recognition*, pp. 11148–11156, 2020.
- [23] J. Lv, K. Hu, J. Xu, Y. Liu, X. Ma, and X. Zuo, "Clins: Continuous-time trajectory estimation for lidar-inertial system," in *2021 IEEE/RSJ International Conference on Intelligent Robots and Systems (IROS)*, pp. 6657–6663, IEEE, 2021.
- [24] X. Lang, C. Chen, K. Tang, Y. Ma, J. Lv, Y. Liu, and X. Zuo, "Coco-lic: continuous-time tightly-coupled lidar-inertial-camera odometry using non-uniform b-spline," *IEEE Robotics and Automation Letters*, 2023.
- [25] J. Zhang, M. Kaess, and S. Singh, "On degeneracy of optimization-based state estimation problems," in *2016 IEEE International Conference on Robotics and Automation (ICRA)*, pp. 809–816, IEEE, 2016.
- [26] A. Hinduja, B.-J. Ho, and M. Kaess, "Degeneracy-aware factors with applications to underwater slam," in *2019 IEEE/RSJ International Conference on Intelligent Robots and Systems (IROS)*, pp. 1293–1299, IEEE, 2019.
- [27] R. Ren, H. Fu, H. Xue, X. Li, X. Hu, and M. Wu, "Lidar-based robust localization for field autonomous vehicles in off-road environments," *Journal of Field Robotics*, vol. 38, no. 8, pp. 1059–1077, 2021.
- [28] J. Nubert, E. Walther, S. Khattak, and M. Hutter, "Learning-based localizability estimation for robust lidar localization," in *2022 IEEE/RSJ International Conference on Intelligent Robots and Systems (IROS)*, pp. 17–24, IEEE, 2022.
- [29] C. Yang, Z. Chai, X. Yang, H. Zhuang, and M. Yang, "Recognition of degradation scenarios for lidar slam applications," in *2022 IEEE International Conference on Robotics and Biomimetics (ROBIO)*, pp. 1726–1731, IEEE, 2022.
- [30] W. Zhen and S. Scherer, "Estimating the localizability in tunnel-like environments using lidar and uwb," in *2019 International Conference on Robotics and Automation (ICRA)*, pp. 4903–4908, IEEE, 2019.
- [31] T. Tuna, J. Nubert, Y. Nava, S. Khattak, and M. Hutter, "X-icp: Localizability-aware lidar registration for robust localization in extreme environments," *IEEE Transactions on Robotics*, 2023.
- [32] J. Yin, A. Li, T. Li, W. Yu, and D. Zou, "M2dgr: A multi-sensor and multi-scenario slam dataset for ground robots," *IEEE Robotics and Automation Letters*, vol. 7, no. 2, pp. 2266–2273, 2021.
- [33] T.-M. Nguyen, S. Yuan, M. Cao, Y. Lyu, T. H. Nguyen, and L. Xie, "Ntu viral: A visual-inertial-ranging-lidar dataset, from an aerial vehicle viewpoint." *The International Journal of Robotics Research*, vol. 41, no. 3, pp. 270–280, 2022.